Wavelength control in high-gain harmonic generation seeded free-electron lasers

F. Sottocorona,[*] G. Perosa,[*] E. Allaria, A. Brynes, M. B. Danailov, G. De Ninno,[†] S. Di Mitri, D. Garzella, G. Penco, C. Spezzani, and L. Giannessi[‡]

Elettra-Sincrotrone Trieste S.C.p.A, 34149 Basovizza, Italy

(Received 28 March 2023; accepted 16 August 2023; published 12 September 2023)

The basic theory of free-electron lasers (FELs) indicates that the output wavelength of a seeded FEL operated in the high-gain harmonic generation (HGHG) configuration is determined by the wavelength of the seed laser and light is emitted when the undulators are tuned to an exact harmonics of the seed laser. In a realistic case, when taking into account the electron beam imperfections and the finite bandwidths of the seed and of the amplification process, the output wavelength is influenced by these factors and can deviate from the exact harmonic resonance. These effects are responsible for the small wavelength fluctuations of the FEL pulses but can also be exploited for an accurate FEL wavelength tuning. In this work, we show how the dispersive section, the curvature of the electron beam longitudinal phase-space and frequency pulling can influence the FEL wavelength and can be, in principle, used to control it. Furthermore, we show how one can reconstruct the electron beam longitudinal phase-space from the analysis of the FEL wavelength sensitivity to the seed laser delay with respect to the beam arrival time.

DOI: 10.1103/PhysRevAccelBeams.26.090702

I. INTRODUCTION

Free electron lasers (FELs) have reached a high level of development in recent years, the spectral range covers continuously the VUV, soft and hard x rays, the power reaches the multi-GW to TW level [1–7], the pulse duration is tuneable and can be reduced down to few hundreds of as [8]. Synchronized multiple pulses of different colors can be implemented in pump and probe experiments [8–11]; the pulse polarization [12–14], as well as the phase and amplitude of the radiation can be controlled at an unprecedented level (see, e.g., [15]); frequency synthesis may be exploited to shape the pulse according to specific experimental needs [16]. Some of these features are enabled by seeding the FEL amplifier with an external optical laser in the so-called high-gain harmonic generation (HGHG) scheme [17]: an external laser modulates the density of the electron beam and the modulated beam emits light upshifted in frequency in a radiator tuned at one of the higher harmonics of the seed. The main features of the seed pulse, such as its amplitude and phase, are transferred to the FEL pulse and control the properties of the output radiation. The seeded FEL FERMI [4], as an example, has some of these unique characteristics, such as the fine spectral tunability and wavelength stability required to probe narrow resonances (see Fig. 1) and the coherence properties at higher orders typical of optical lasers [18].

The output wavelength of a seeded FEL is determined by the fact that constructive interference from periodically bunched electrons occurs at the harmonics λ_s/n of the seed laser wavelength λ_s. An efficient FEL emission is produced when the periodicity of the density modulation matches the resonance condition in the amplifier, i.e.,

$$\lambda_s/n = \lambda_{\mathrm{res}}, \tag{1}$$

where

$$\lambda_{\mathrm{res}} = \frac{\lambda_u}{2\gamma_0^2}(1 + a_w^2), \tag{2}$$

and where λ_u is the undulator period, a_w the undulator strength and γ_0 is the energy of the beam in $m_e c^2$ units, (m_e is the electron mass and c the speed of light in vacuum). This condition contributes to the wavelength stability of the seeded FEL [19], that unlike a self-amplified spontaneous emission amplifier [20], is not dominated by the beam energy fluctuations through the parameter γ_0 in Eq. (2). In practice, several phenomena occur in the HGHG harmonic conversion process that can slightly shift the output

[*]Also at Università degli Studi di Trieste, Italy.

[†]Also at University of Nova Gorica, 5000 Nova Gorica, Slovenia.

[‡]Also at Istituto Nazionale di Fisica Nucleare, Laboratori Nazionali di Frascati, 00044 Frascati, Roma, Italy.

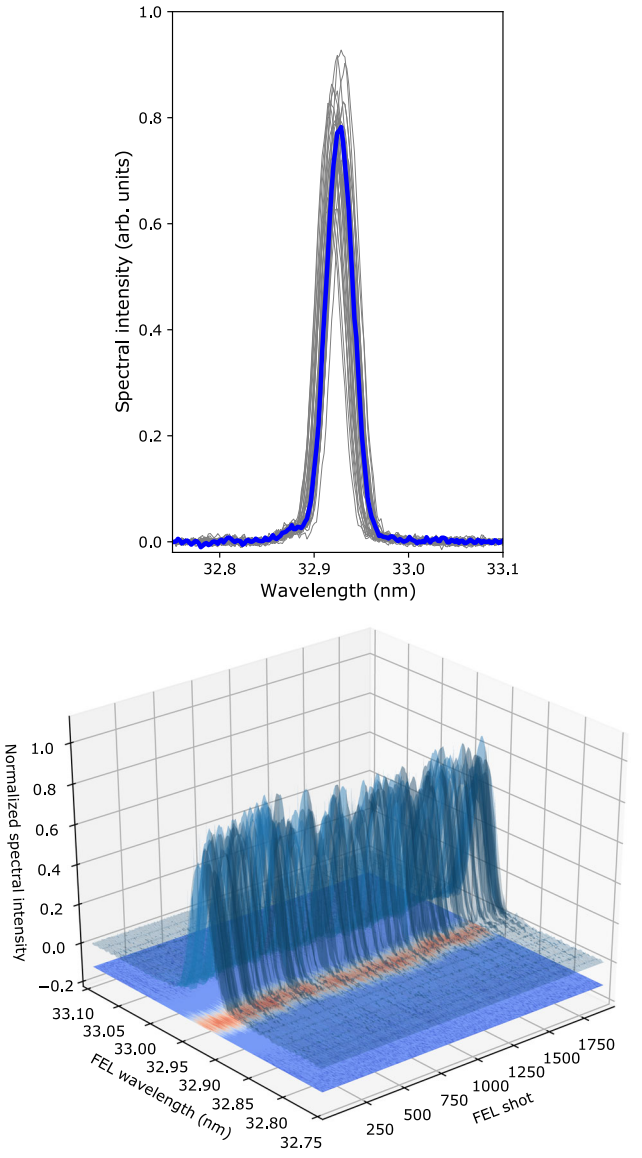

FIG. 1. Example of the stability achievable on FERMI FEL-1: a sequence of 15 spectra (top) randomly selected from the collection (bottom) is shown. The blue thick line represents the average spectrum.

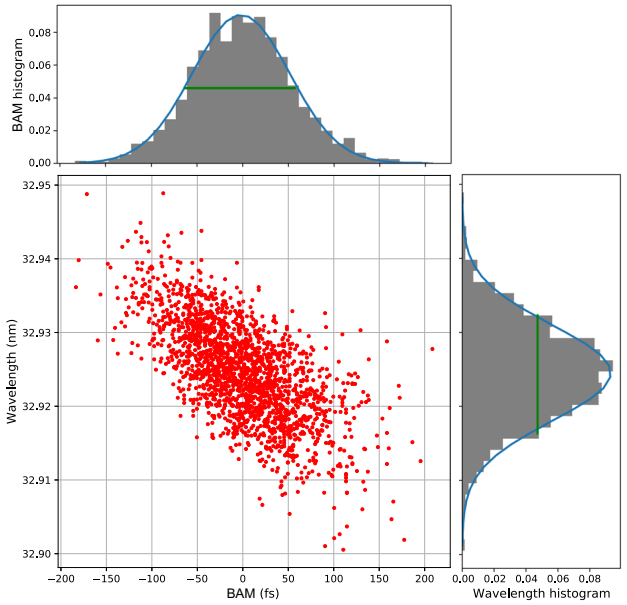

FIG. 2. Correlation between the FEL central wavelength (0.0065 nm rms) and the electron beam arrival time measured with a beam arrival monitor (BAM, acronym of beam arrival monitor), retrieved from the 2000 samples of spectra shown in Fig. 1. The distribution of 2000 samples has a temporal dispersion of 55 fs (rms); the correlation factor is 67%.

wavelength from the exact integer harmonic of the seed. As an example, in Fig. 2 we show the correlation between the distribution of the FEL central emission wavelength and the arrival time of the seed pulse at the electron bunch. The clear correlation indicates the deterministic nature of the fluctuations and shows that even in a seeded FEL, the central emission wavelength is influenced by the local electron beam properties, which in the case shown in Fig. 2 are dependent on the seed arrival time. Even though these fluctuations are, at FERMI, typically smaller than the FEL bandwidth and normally do not interfere with the user operation of the facility, an understanding of their origin is important. In addition, correlation plots similar to the one shown in Fig. 2 may be used as a diagnostic tool for understanding the properties of the electron beam and of the emitted radiation. One example is the reconstruction and control of the frequency chirp of the emitted pulses (see, e.g., [21,22]).

In this work, we analyze the role of the electron beam longitudinal phase space in determining the wavelength stability of an FEL from a theoretical and experimental point of view. In the next section we analyze the main factors that determine the central wavelength in a seeded FEL. In Sec. III, the model proposed in Sec. II is compared to experimental data acquired at FERMI. Finally in Sec. IV, the model is used to reconstruct the longitudinal phase space of the beam, using a simple scan of the relative delay between electrons and seed, a routine operation carried out at FERMI during the FEL optimization.

II. HIGH-GAIN HARMONIC GENERATION AND CENTRAL EMISSION WAVELENGTH

Correlations are routinely used in the optimization of FERMI [23]. Correlations can show critical conditions, detuned parameters, such as resonances or delays. The correlation plot in Fig. 2 suggests that the longitudinal energy distribution of the electron beam plays a key role in the central FEL emission wavelength. A typical measurement of the electron beam phase-space obtained at FERMI at the end of the linac (see Fig. 3) is shown in Fig. 4 (top). Such a measurement is obtained by dispersing the beam temporally with a transverse rf deflector [24], and in

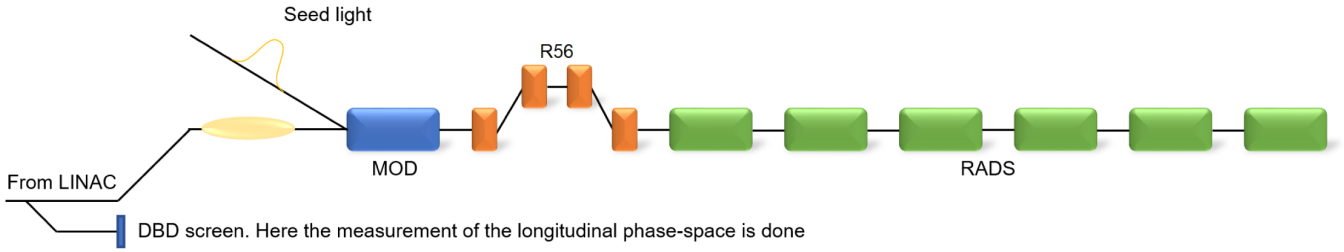

FIG. 3. Layout of the FERMI FEL-1 HGHG FEL. The measurement of the phase-space is carried out at the diagnostic beam dump (DBD) at the end of the linac, by combining the effects of a horizontal bending magnet and a vertical radio-frequency deflector.

energy, by a magnetic spectrometer, installed in sequence along the beam propagation axis. The plot shows a strong correlation in the energy-time distribution. Fig. 4 (bottom), reports the beam current and energy profile, reconstructed from the analysis of Fig. 4 (top).

In a seeded HGHG FEL, at first the beam is modulated in energy by the interaction between the electrons and the external seed in a first undulator resonant with the seed, known as a modulator. The period of this modulation is equal to the wavelength λ_s of the seed. Second, the energy modulation is converted into a density modulation in a dispersive chicane. As a result, the electron beam is modulated in microbunches that will emit in phase either

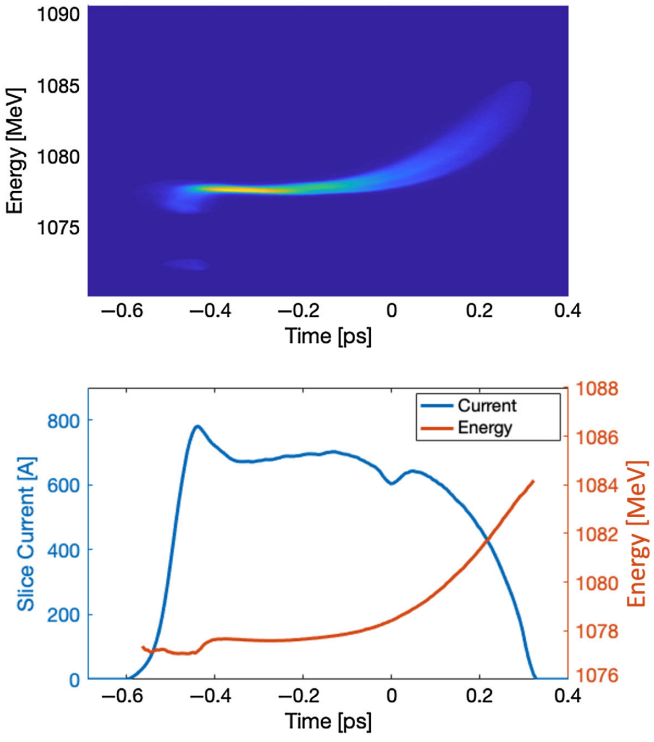

FIG. 4. The top plot represents the beam snapshot on the CCD after the dispersive effect of the bending magnet (vertical plane) and the time-dependent kick impressed by the radio-frequency deflector (horizontal axis). Fits of the average current (blue) and energy (red) as functions of the deflector phase (time) are shown in the bottom plot.

at the modulation wavelength or at one of its higher order harmonics, depending on the resonance condition that matches the resonance of a final amplifier. The dispersive section has also an effect on the electron bunch distribution, when the beam energy varies as a function of longitudinal position along the bunch (i.e., an energy chirp), as is the case shown in Fig. 4. The beam is indeed compressed or decompressed depending on the sign of the energy-phase correlation of the beam distribution at the seed pulse position. The periodicity of the energy modulation imposed on the beam before the dispersive section is therefore "blue" shifted or "red" shifted by the dispersive element, depending on the energy-time correlation. In particular, linear compression of the beam is determined by the linear term of this energy-time dependence. The harmonic coherent emission will no longer occur exactly at λ_s/n, but rather at the shifted wavelength

$$\lambda_{\mathrm{HGHG}} = \frac{\lambda_s/n}{1 - \frac{R_{56}}{\gamma(t)}\frac{d\gamma(t)}{dt}}, \tag{3}$$

where $\gamma(t)$ is the temporal energy profile, R_{56} is the longitudinal dispersion (we assume negative longitudinal dispersion for a magnet compressing a beam with $d\gamma/dt > 0$), and λ_{HGHG} is the wavelength of the density modulation after the dispersive section. Equation (3) shows that it is also possible to fine-tune the wavelength of the coherent bunching at a fixed seed wavelength, by acting on the R_{56}, or on the linear chirp of the electron beam distribution [25]. However, for an optimized FEL, the R_{56} and the beam linear chirp cannot be both arbitrarily tuned. The first determines the bunching amplitude at a given seed intensity: a large variation of R_{56} would lead to a reduction of bunching (low FEL intensity) or to over-bunching [26,27]; the second is determined by longitudinal wake-fields and by the beam dynamics in the linac: changes in these parameters may reduce the quality of the FEL beam, or may even not be achievable. However, the seed is typically much shorter than the electron beam and due to the typical quadratic chirp of the energy vs z distribution (see Fig. 4) the linear chirp component of the seeded electrons can be varied by properly selecting the relative timing between the seed laser and the electron beam.

This parameter can be therefore used for a fine wavelength tuning.

From the data in Fig. 4 (bottom), we observe that a seed arrival time variation of 200 fs could explore a region where the sign of the energy-time correlation of the distribution may change and where the beam energy may vary by 1–2 MeV. FEL amplification occurs in a spectral range corresponding to the amplifier gain bandwidth centered, to a first approximation, around the resonance condition in Eq. (2). The gain bandwidth is estimated from the Pierce parameter ρ [20]: in the case of FERMI ρ is of the order of few 10^{-3}. The range of the wavelength tuning, without changing the undulator strength a_w, is therefore pretty small: in terms of beam energy ($\delta\omega = 2\delta\gamma$), at 1 GeV the gain spectral width corresponds to an energy detuning of a few MeV (FWHM). When the bunching wavelength (λ_{HGHG}) does not match the resonant wavelength (λ_{res}), the intensity drops and a frequency pulling effect slightly shifts the emission wavelength according to the relation [28]:

$$\lambda_{\mathrm{FEL}} = \left[\frac{1}{\lambda_{\mathrm{HGHG}}} - \left(\frac{1}{\lambda_{\mathrm{HGHG}}} - \frac{1}{\lambda_{\mathrm{res}}}\right)\frac{\sigma_b^2}{\sigma_b^2 + \sigma_u^2}\right]^{-1}, \quad (4)$$

where λ_{FEL} refers to the final FEL wavelength, and where σ_u and σ_b are the (rms) width of the gain process (of the order of the Pierce parameter ρ) and the electron modulation (rms) spectral bandwidth, respectively. The parameter σ_b corresponds to the relative bandwidth of the spectrum of the beam bunching factor temporal distribution $b_n(t)$ that results from the modulation imposed on the beam by the seed. In the hypothesis of a smooth electron beam distribution and a Fourier transform limited seed laser field, σ_b can be estimated from the pulse duration of the seed [29]. In an optimized HGHG FEL, according to the analysis in [29], σ_b is proportional to the seed spectral bandwidth σ_s and scales with the harmonic order as

$$\sigma_b \simeq \frac{6}{7}\sigma_s n^{-2/3}. \quad (5)$$

Reducing the emission bandwidth is one of the reasons for seeding an FEL amplifier, in this case, we expect σ_b to be small with respect to σ_u. From the relation Eq. (4), we see that, if $\sigma_b \ll \sigma_u$ then the wavelength shift is small and the final FEL wavelength is determined by the bunching modulation wavelength. If instead $\sigma_b \gg \sigma_u$, the FEL wavelength shifts toward λ_{res}. This happens when the FEL is seeded with very short pulses, or, e.g., in a superradiant cascade [30], where the FEL saturation process is used to shorten the duration of the FEL pulse. This may also happen in a more typical HGHG FEL configuration operating with a long seed, but where beam modulations, such as those induced by the microbunching instability, broaden the spectrum of the beam density modulation $b_n(t)$ [31–33]. In summary, the FEL output wavelength depends on the undulator resonance condition, on the seed laser parameters and on the energy chirp of the longitudinal phase space distribution. The first two correspond to typically well-known parameters determined by the settings of the seed laser, of the undulator and by the electron beam energy; conversely the local energy-time slope of the phase space distribution requires a specific measurement with a deflecting cavity combined with an electron energy spectrometer, which may be not available in front of the undulator.

The typical electron energy distribution at FERMI is characterized by high-order chirp components whose origin is mainly due to the combination of radiofrequency curvature and longitudinal wakefield effects. To a first approximation, we represent the average dependence of the beam energy on the longitudinal coordinate, $\gamma(t)$ as a third order polynomial expanded around a specific point t_0

$$\gamma(t) = \chi_0 + \chi_1(t - t_0) + \frac{\chi_2}{2}(t - t_0)^2 + \frac{\chi_3}{6}(t - t_0)^3, \quad (6)$$

where χ_0 corresponds to the resonance energy at $t = t_0$ and χ_i, with $i > 0$, are the linear, quadratic, and cubic chirp components of the expansion around t_0. As an example, we plot in Fig. 5 the energy-time profile of a beam with typical parameters that could be measured from a FERMI electron beam distribution. The resonant wavelength [defined in Eq. (2)] along the electron bunch is therefore dependent on its energy, as shown in Fig. 6. A different setting of the undulator strength a_w controlled by the gap of the radiators is equivalent to the introduction of an energy detuning; the different lines in Fig. 6 correspond to changes of the reference electron beam energy (χ_0) of ± 2 MeV, with steps of 0.5 MeV.

In a SASE FEL, Eq. (2) sets the resonance condition; radiation is emitted by the entire bunch, weighted by the local amplification efficiency that depends on current and

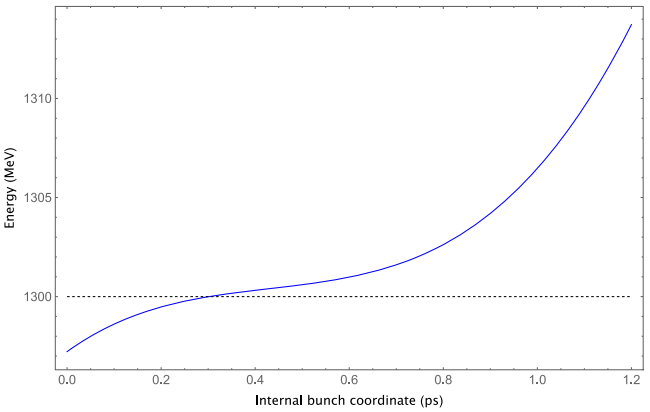

FIG. 5. Example of a possible energy-time profile of beam phase space from Eq. (6). Here we have used $\chi_0 = 1300$ MeV, $\chi_1 = 4$ MeV/ps, $\chi_2 = -20$ MeV/ps^2, and $\chi_3 = 150$ MeV/ps^3. The black dashed line represents the energy χ_0 at $t = t_0$.

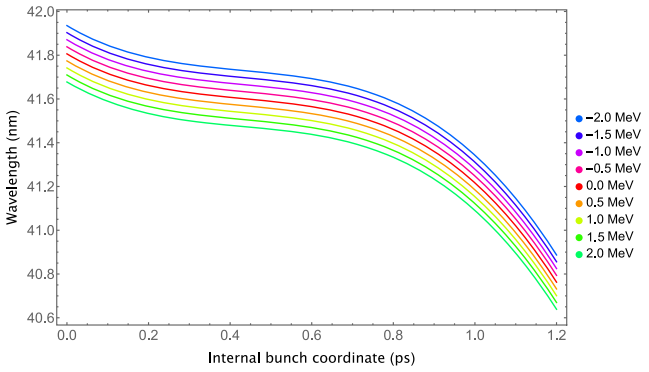

FIG. 6. Behavior of λ_{res} from Eq. (2) as a function of the local beam energy assuming the energy-phase distribution shown in Fig. 5. The colored lines indicate changes of the reference electron beam energy (χ_0) in steps of 0.5 MeV. The undulator has a period length $\lambda_u = 5.52$ cm, $K = 2.954$ and circular polarization mode.

on the distribution of energy spread and emittances. In a seeded FEL, the electron modulation is determined by the seed wavelength, but the final emission wavelength is determined by the combined effect of the seed modulation, the modulation compression, Eq. (3) and by the frequency pulling Eq. (4), to be estimated in the time interval of the beam interacting with the seed.

In Fig. 7, the effect of the dispersive section is shown: Eq. (3) is used to calculate the bunching wavelength at the sixth harmonic of a seed of wavelength $\lambda_{\mathrm{seed}} = 250.0$ nm, corresponding to an emission wavelength of about 41.66 nm. The effect of a linear energy chirp $\gamma(t) = \chi_0 + \chi_1(t - t_0)$ is that of introducing an offset in the emission wavelength

$$\lambda_{\mathrm{HGHG}} \simeq \frac{\lambda_s}{n}\left(1 + R_{56}\frac{\chi_1}{\chi_0}\right). \tag{7}$$

Due to the local variation of the chirp, the bunching wavelength depends on the longitudinal coordinate along

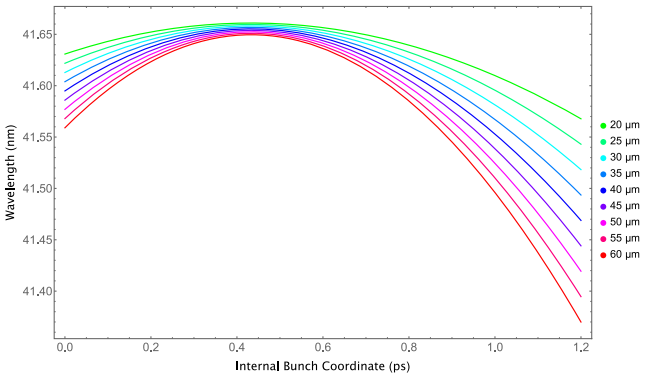

FIG. 7. Behavior of λ_{HGHG} from Eq. (3) along the bunch with the energy-phase correlation shown in Fig. 5, for different values of longitudinal dispersion R_{56}.

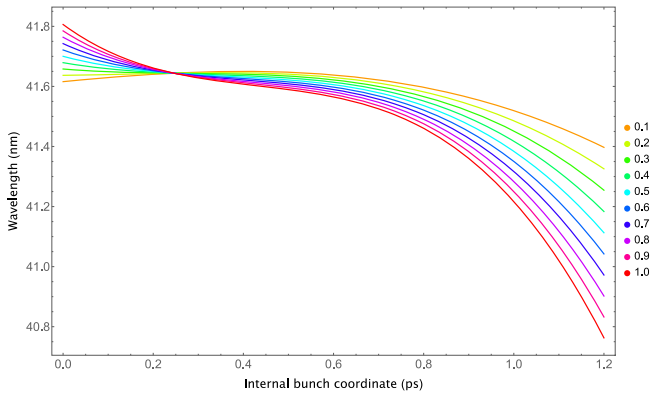

FIG. 8. Behavior of λ_{FEL} from Eq. (4) along the bunch with the energy-phase correlation shown in Fig. 5, for different values of the frequency pulling coefficient FP.

the beam; a change in the dispersion R_{56} induces a time-dependent shift of the output wavelength. The minimum shift corresponds to the position along the bunch where $d\gamma/dt$ is at a minimum, the larger is the strength of the dispersive section, the larger the shift.

We now consider the frequency pulling effect. We can see from Eq. (4) that the final wavelength λ_{FEL} is the result of an interplay between the two wavelengths corresponding to the resonance relation and the bunching modulation, after the compression in the dispersive section. The behavior of λ_{FEL} as a function of the frequency pulling coefficient $\mathrm{FP} = \sigma_b^2/(\sigma_b^2 + \sigma_u^2)$ is shown in Fig. 8, given a fixed value ($R_{56} = 40$ μm) for the longitudinal dispersion and the same longitudinal phase space as that shown in Fig. 5. In the case of a narrowband seed, i.e., low values of FP, the FEL wavelength profile is dominated by the seed and the emitted wavelength follows λ_{HGHG} plotted in Fig. 7 (orange line in Fig. 8). For large bandwidth, e.g., short seed pulses corresponding to large values of FP instead, the FEL wavelength follows the resonant wavelength of Fig. 6 (red line in Fig. 8). For an intermediate value of FP, the final wavelength is the result of a combined effect.

III. EXPERIMENTAL DATA

The previous analysis was verified experimentally at FERMI. The seed laser was tuned to 250 nm and the FEL HGHG conversion was set to harmonic ten. For a given longitudinal phase-space, the behavior of the FEL wavelength vs the seed delay can be determined with the equations described in the previous section. The seed delay scan can also be used to fine-tune the values of the FEL wavelength by selecting the internal coordinate of the seeded part. In Fig. 9, the FEL central wavelength was measured during a scan of the seed temporal delay, with the undulator gaps set at three different resonances. The jitter between the arrival time of the electrons and the seed is measured by a beam arrival monitor; the typical shot-to-shot jitter is about 40 fs, shorter than the duration of the

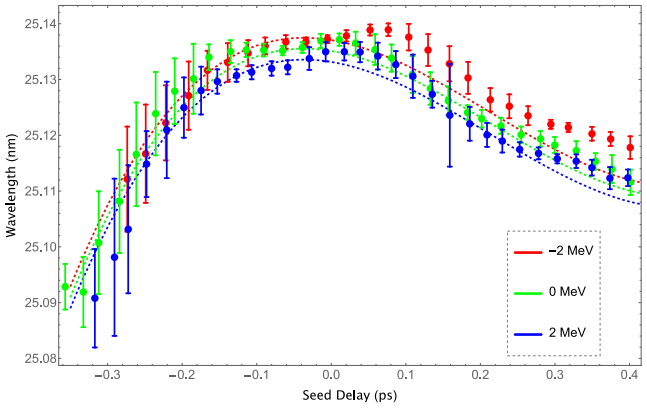

FIG. 9. Comparison between the central wavelength resulting from a seed delay scan and the combined effect of pulling Eq. (4) and compression Eq. (3) assuming the energy-time correlation Eq. (6) with $\chi_0 = 1297$ MeV, $\chi_1 = 6$ MeV/ps, $\chi_2 = 12$ MeV/ps^2, $\chi_3 = 300$ MeV/ps^3, and $\chi_4 = -1400.0$ MeV/ps^4. The three colors correspond to an energy detuning of ± 2 MeV. The detuning is achieved by effectively tuning the undulator strength off-resonance by an equivalent K parameter shift.

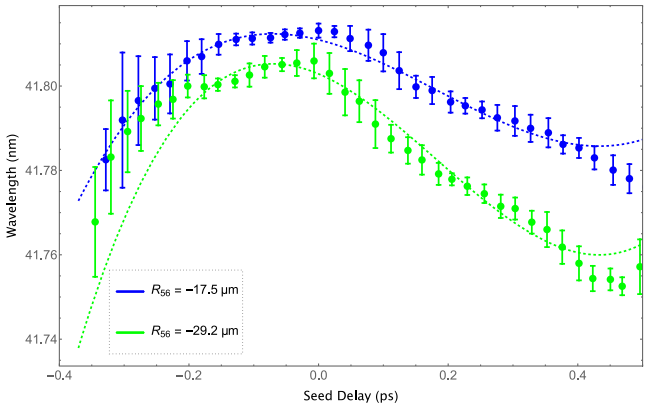

FIG. 10. Matching behavior between the seed scan acquisitions and the theoretical solution at harmonic $n = 6$, for two different dispersive section values. The phase space parameters are the same as in Fig. 9. At harmonic six we have $\rho \simeq 2 \times 10^{-3}$, $\sigma_b \sim 3.9 \times 10^{-4}$ corresponding to FP $\simeq 0.036$.

seed (of the order of 100 fs). The beam and undulator parameters allow us to estimate the ρ_{3D} parameter [34] for the configuration $(\rho_{3D} \simeq 1.7 \times 10^{-3})$. The seed relative spectral width σ_s is directly measured (1.5×10^{-3}), corresponding (at harmonic 10) to $\sigma_b \simeq 2.8 \times 10^{-4}$, the seed duration is approximately 100 fs (FWHM). This allows us to estimate the wavelength shift due to frequency pulling, FP $= 0.026$. The dashed lines represent the prediction using a suitable energy-time distribution $\gamma(t)$ (see the caption of Fig. 9) and Eqs. (2)–(4) allow us to fit the distribution of λ_{FEL} as a function of the delay. In the case considered, the parameter FP is small, the wavelength shift is dominated by the compression effect and the resonance has a modest influence on the final wavelength, the curves in the range ± 2 MeV are almost overlapping. The quadratic and cubic chirps are responsible for the variation of the FEL wavelength vs the seed delay. The linear chirp introduces an offset on the emitted wavelength (a vertical offset in the plot), but does not give a dependence of the resonance on the seed actuator position. In order to identify uniquely the contribution of the linear chirp simply using the response of the FEL vs the seed delay scan, an absolute spectrometer calibration and a precise calibration of the undulator resonance is required.

The strength of the dispersive section also plays a role in the determination of the final FEL wavelength. This was verified by measuring the central FEL wavelength vs seed delay for different values of R_{56}. The plot in Fig. 10 shows the central wavelength vs the delay with the seed laser tuned at 250 nm and the undulators at harmonic $n = 6$ of the seed. The dashed lines in Fig. 10 show the results of the theoretical analysis, assuming the same beam distribution used for Fig. 9. The two measurements were done with similar beam parameters and the overall behavior is qualitatively well reproduced. The main differences arise at the boundaries of the window, for the low number of expansion terms in the polynomial Eq. (6) and for the presence, on the beam head (left side of the plot) of microbunching instability that broadens σ_b and increases the frequency pulling effect. In addition to that, when the delay is large, also the FEL intensity decreases because of resonance detuning and increased energy spread. The measurements based on the spectral measurements become less accurate.

IV. PHASE-SPACE RECONSTRUCTION

The fact that the same beam parameters allowed us to reproduce qualitatively both Figs. 9 and 10 suggests that the dependence of the FEL wavelength on the seed delay can be exploited by inverting Eq. (3) to determine the energy-time distribution of the electron beam itself. In a condition of low FP parameter and with the resonance set reasonably close to the undulator resonance, the seeded FEL wavelength is determined by Eq. (3). Interpolating the behavior of the wavelength while varying the seed delay we can reconstruct the function $\gamma(t)$. The average beam energy as a function of the coordinate along the bunch $\gamma(t)$ is given by $(\gamma_0 = \gamma(t_0))$

$$\gamma(t) = \gamma_0 \exp\left[\frac{1}{R_{56}} \int_{t_0}^{t} \left(1 - \frac{\lambda_{\mathrm{seed}}/n}{\lambda_{\mathrm{FEL}}(t')}\right) dt'\right]. \qquad (8)$$

In Fig. 11, we show the reconstructed function $\gamma(t)$ from two scans of the seed delay at two different values of the dispersive section. The two reconstructed phase-spaces are in good agreement, except for a discrepancy on the bunch head (left side of the plot) where typically the distribution nonlinearities, energy spread and coherent synchrotron radiation effects are larger. The full phase space reconstruction is affected by the calibration and sensitivity of the

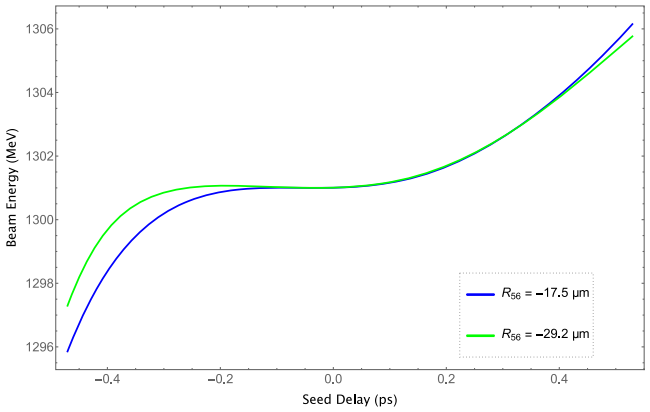

FIG. 11. Phase-space reconstructed from the seed scans of the dispersive section.

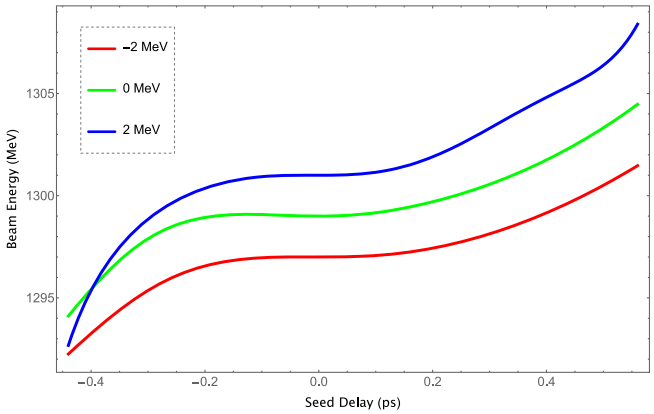

FIG. 12. Phase-space reconstructed from the seed scans of the resonance condition.

spectrometer. The spectrometer has a relative resolution of 10^{-5} [35], 1 order of magnitude smaller than the FEL rms spectral width (few 10^{-4}). Locally, due to microbunching instability, we observe an increase of the shot to shot jitter of the central wavelength. Here the measurement by itself is still accurate, it is the underlying phase space that is changing shot-to-shot in a way sensed by the harmonic conversion and by the amplification process. There is a systematic error in the spectral measurement, that depends on the absolute calibration of the spectrometer. The error depends mostly on the lack of an input slit at the instrument, that is affected by the light propagation angle. The instrument can be absolutely calibrated when required using know resonances, but this was not done for this experiment. An uncertainty in the spectrometer calibration $\delta\lambda$ corresponds to an uncertainty $\delta\chi_1$ in the linear energy chirp χ_1 [see Eq. (7)]. Inverting Eq. (7), we get

$$\delta\chi_1 = \frac{\gamma_0}{R_{56}}\frac{n\delta\lambda}{\lambda_s}. \tag{9}$$

In the operating conditions ($\delta\lambda \simeq \pm 0.1$ nm, $\lambda_s/n \simeq$ 41 nm, $\gamma_0 \simeq 2540$, $R_{56} \simeq 30$ μm), this corresponds to an uncertainty of the linear chirp $\delta\chi_1 \simeq \pm 19$ keV/fs. An accurate measurement of both the FEL and the seed absolute wavelength is required for the precise determination of the linear chirp term. Nevertheless, the method allows the determination of the higher order components of the electron distribution at the seed position, which are relevant in the reconstruction of the final FEL pulse temporal chirp distribution [27]. Figure 12 represents the phase space that is reconstructed from the delay scans done by varying the undulator strength parameter corresponding to a shift of the resonant energy of $(0, \pm 2)$ MeV. Apart from the energy offset, the main features of the electron beam energy distribution are correctly reproduced: in the region surrounding t_0, the behavior of the three lines is very similar. This shows that the higher order chirp components (χ_2, χ_3) can be determined, even with a limited knowledge of the absolute beam energy (χ_0) and of the linear term (χ_1).

V. CONCLUSIONS

The local characteristics of the longitudinal phase-space distribution of the electron beam affect the FEL emission wavelength. A shift in the arrival time of the electron bunch corresponds to a shift of the seeded region and allow the measurement some of these characteristics. In this work, we have shown how the central wavelength of a HGHG seeded FEL is affected by three main contributions: the resonance condition, the strength of the dispersive section and the gain, via frequency pulling. These relations allow to predict the impact of the time jitter on the FEL wavelength stability, and the dependence of the FEL emission wavelength on the seed delay can be used to reconstruct the longitudinal phase-space in the region defined by the seed delay scan. Knowledge of the high-order components of the electron beam phase space curvature at the position of the seed can be implemented to measure the frequency chirp of the FEL pulse induced by this curvature. Finally, the local wavelength shift can also give information regarding the spectral width of the bunching factor, providing indirect time-resolved information about the microbunching instability heated region of the electron beam.

ACKNOWLEDGMENTS

The authors very much appreciate enlightening discussions with Dr. C. Callegari and with Dr. Primoz Rebernik.

[1] W. Ackermann *et al.*, Nat. Photonics **1**, 336 (2007).
[2] P. Emma, R. Akre, J. Arthur, R. Bionta, C. Bostedt, J. Bozek, A. Brachmann, P. Bucksbaum, R. Coffee, F.-J. Decker *et al.*, Nat. Photonics **4**, 641 (2010).

[3] T. Ishikawa, H. Aoyagi, T. Asaka, Y. Asano, N. Azumi, T. Bizen, H. Ego, K. Fukami, T. Fukui, Y. Furukawa *et al.*, Nat. Photonics **6**, 540 (2012).
[4] E. Allaria *et al.*, J. Synchrotron Radiat. **22**, 485 (2015).
[5] H.-S. Kang *et al.*, Nat. Photonics **11**, 708 (2017).
[6] E. Prat *et al.*, Nat. Photonics **14**, 748 (2020).
[7] W. Decking, Nat. Photonics **14**, 391 (2020).
[8] A. A. Lutman, M. W. Guetg, T. J. Maxwell, J. P. MacArthur, Y. Ding, C. Emma, J. Krzywinski, A. Marinelli, and Z. Huang, Phys. Rev. Lett. **120**, 264801 (2018).
[9] E. Allaria *et al.*, Nat. Commun. **4**, 2476 (2013).
[10] A. Marinelli, D. Ratner, A. A. Lutman, J. Turner, J. Welch, F. J. Decker, H. Loos, C. Behrens, S. Gilevich, A. A. Miahnahri, S. Vetter, T. J. Maxwell, Y. Ding, R. Coffee, S. Wakatsuki, and Z. Huang, Nat. Commun. **6**, 6369 (2015).
[11] E. Prat, P. Dijkstal, E. Ferrari, R. Ganter, P. Juranić, A. Malyzhenkov, S. Reiche, T. Schietinger, G. Wang, A. A. Haddad, S. Augustin, C. Bostedt, G. Knopp, J. Knurr, A. S. Morillo-Candas, Z. Sun, and K. Schnorr, Phys. Rev. Res. **4**, L022025 (2022).
[12] E. Allaria *et al.*, Phys. Rev. X **4**, 041040 (2014).
[13] E. Hemsing, A. Knyazik, M. Dunning, D. Xiang, A. Marinelli, C. Hast, and J. B. Rosenzweig, Nat. Phys. **9**, 549 (2013).
[14] G. De Ninno *et al.*, Nat. Photonics **14**, 554 (2020).
[15] K. C. Prince *et al.*, Nat. Photonics **10**, 176 (2016).
[16] P. K. Maroju, C. Grazioli, M. Di Fraia, M. Moioli, D. Ertel, H. Ahmadi, O. Plekan, P. Finetti, E. Allaria, L. Giannessi *et al.*, Nature (London) **578**, 386 (2020).
[17] L. H. Yu, Phys. Rev. A **44**, 5178 (1991).
[18] O. Y. Gorobtsov, G. Mercurio, F. Capotondi, P. Skopintsev, S. Lazarev, I. A. Zaluzhnyy, M. B. Danailov, M. Dell'Angela, M. Manfredda, E. Pedersoli, L. Giannessi, M. Kiskinova, K. C. Prince, W. Wurth, and I. A. Vartanyants, Nat. Commun. **9**, 4498 (2018).
[19] E. Allaria *et al.*, Nat. Photonics **6**, 699 (2012).
[20] E. L. Saldin, E. A. Schneidmiller, and M. V. Yurkov, *The Physics of Free Electron Lasers* (Springer Berlin, Heidelberg, 2000).
[21] D. Meshulach and Y. Silberberg, Nature (London) **396**, 239 (1998).
[22] S. Nandi *et al.*, Nature (London) **608**, 488 (2022).
[23] G. Gaio, N. Bruchon, M. Lonza, and L. Saule, in *Proceedings of the 16th International Conference on Accelerator and Large Experimental Control Systems (ICALEPCS'17), Barcelona, Spain, 2017* (JACoW, Geneva, 2018), TUMPA07, pp. 352–356, https://doi.org/10.18429/JACoW-ICALEPCS2017-TUMPA07.
[24] P. Craievich, M. Petronio, S. G. Biedron, D. Castronovo, M. D. Forno, S. D. Mitri, N. Faure, D. L. Civita, G. Penco, L. Rumiz, L. Sturari, R. Vescovo, and D. Wang, IEEE Trans. Nucl. Sci. **62**, 210 (2015).
[25] T. Shaftan and L. H. Yu, Phys. Rev. E **71**, 046501 (2005).
[26] M. Labat, N. Joly, S. Bielawski, C. Szwaj, C. Bruni, and M. E. Couprie, Phys. Rev. Lett. **103**, 264801 (2009).
[27] D. Gauthier, P. R. Ribič, G. De Ninno, E. Allaria, P. Cinquegrana, M. B. Danailov, A. Demidovich, E. Ferrari, L. Giannessi, B. Mahieu, and G. Penco, Phys. Rev. Lett. **115**, 114801 (2015).
[28] E. Allaria, G. D. Ninno, and C. Spezzani, Opt. Express **19**, 10619 (2011).
[29] P. Finetti, H. Höppner, E. Allaria, C. Callegari, F. Capotondi, P. Cinquegrana, M. Coreno, R. Cucini, M. B. Danailov, A. Demidovich *et al.*, Phys. Rev. X **7**, 021043 (2017).
[30] N. S. Mirian *et al.*, Nat. Photonics **15**, 523 (2021).
[31] E. Roussel, E. Ferrari, E. Allaria, G. Penco, S. D. Mitri, M. Veronese, M. Danailov, D. Gauthier, and L. Giannessi, Phys. Rev. Lett. **115**, 214801 (2015).
[32] Z. Zhang, R. Lindberg, W. M. Fawley, Z. Huang, J. Krzywinski, A. Lutman, G. Marcus, and A. Marinelli, Phys. Rev. Accel. Beams **19**, 050701 (2016).
[33] G. Marcus, W. M. Fawley, D. Bohler, Y. Ding, Y. Feng, E. Hemsing, Z. Huang, J. Krzywinski, A. Lutman, and D. Ratner, Phys. Rev. Accel. Beams **22**, 080702 (2019).
[34] M. Xie, in *Proceedings Particle Accelerator Conference* (IEEE, New York, 1995), Vol. 1, pp. 183–185.
[35] M. Zangrando, D. Cocco, C. Fava, S. Gerusina, R. Gobessi, N. Mahne, E. Mazzucco, L. Raimondi, L. Rumiz, and C. Svetina, J. Synchrotron Radiat. **22**, 565 (2015).